Moving Contact Lines: Scales, Regimes, and Dynamical Transitions

Jacco H. Snoeijer[1] and Bruno Andreotti[2]

[1]Physics of Fluids Group, MESA+ Institute, University of Twente, 7500AE Enschede, The Netherlands; email: j.h.snoeijer@tnw.utwente.nl, andreotti@pmmh.espci.fr

[2]Laboratoire de Physique et Mécanique des Milieux Hétérogènes, PMMH UMR 7636 ESPCI – CNRS – Université Paris Diderot – Université Pierre et Marie Curie, 75005 Paris, France

Annu. Rev. Fluid Mech. 2013. 45:269–92

The *Annual Review of Fluid Mechanics* is online at fluid.annualreviews.org

This article's doi:
10.1146/annurev-fluid-011212-140734

Keywords

wetting, spreading, wetting transitions, lubrication, contact angle, interface dynamics

Abstract

The speed at which a liquid can move over a solid surface is strongly limited when a three-phase contact line is present, separating wet from dry regions. When enforcing large contact line speeds, this leads to the entrainment of drops, films, or air bubbles. In this review, we discuss experimental and theoretical progress revealing the physical mechanisms behind these dynamical wetting transitions. In this context, we discuss microscopic processes that have been proposed to resolve the moving–contact line paradox and identify the different dynamical regimes of contact line motion.

1. INTRODUCTION

Multiscale: indicates that physical processes at very different length scales are intimately coupled and cannot be separated

Those who have examined the slow motion of droplets on the window of a fast train are aware that a macroscopic flow can be strongly affected by interactions at molecular scales. Namely, the droplets are governed by the wetting dynamics of the contact line, which is the line that separates wet regions from dry regions. This contact line motion is ultimately determined by the physicochemical interactions with the substrate (**Figure 1**): The hydrophobicity of an impacting sphere, which can be altered by a coating of a few nanometers thick, controls the outcome of a macroscopic splash. In the past few decades, understanding and modeling this wetting dynamics have been the subject of intense activity at the forefront of fluid mechanics, chemistry, and engineering. In recent years, the main progress has been on the multiscale nature of the flow and how this gives rise to dynamical transitions such as that shown for the splash in **Figure 1**. In addition, the increasing control over surface properties has led to a wealth of new phenomena, such as superhydrophobicity, whereas the complexity of liquids and their solutes can give rise to intricate patterning and self-assembly (**Figure 2**). In many cases, research is motivated by numerous applications encountered in industrial processes, ranging from oil recovery to imbibition of powders, microfluidics and inkjet printing, to the deposition of pesticides on plant leaves.

In this review, we focus on a single fundamental problem of wetting dynamics: the motion of a contact line over a smooth substrate. We do not touch on other contemporary issues such as superhydrophobic substrates, Marangoni-driven flows, evaporation, and electrowetting, which involve dynamic contact lines in relatively complex situations (for reviews, see Bonn et al. 2009, Craster & Matar 2009, Mugele & Baret 2005, Roach et al. 2008). Rather, we focus on the nature of dynamical wetting transitions that occur at large driving velocities: These transitions lead to the entrainment of films, drops, or air bubbles (**Figure 1**). In many applications (such as coating, painting, and immersion lithography), these entrainment phenomena are crucial limiting factors for industrial processes. From a fundamental perspective, the dynamical wetting transition forms an ideal testing ground for the various models of contact line motion: It provides more complete information than the dynamic contact angle, for example, which is classically used to compare different models.

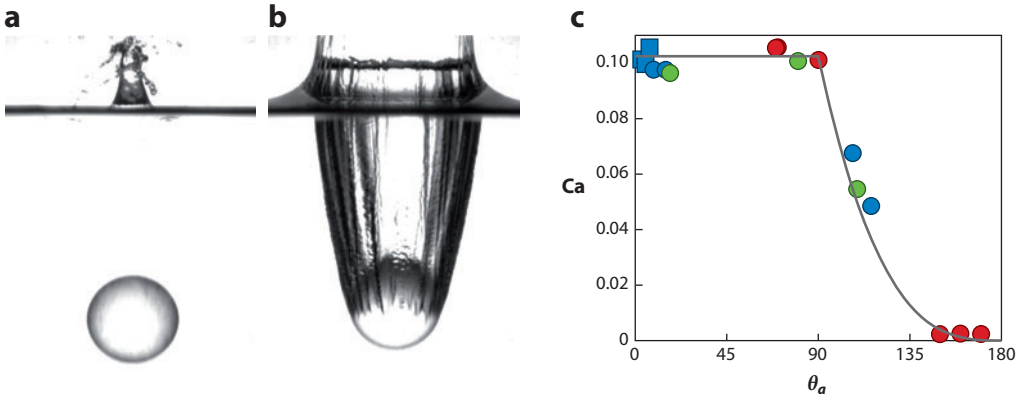

Figure 1

Impact of two spheres differing only in wettability via a nanometric coating on their surface: (*a*) hydrophilic, $\theta_e = 15°$, and (*b*) hydrophobic, $\theta_e = 100°$. (*c*) The threshold capillary number, Ca, for air entrainment is shown as a function of the advancing contact angle θ_a of the impacting body. Data correspond to various sphere diameters (*colors*) and various viscosities (*symbols*). Figure adapted by permission from Macmillan Publishers Ltd: *Nature Physics* (Duez et al. 2007), copyright 2007.

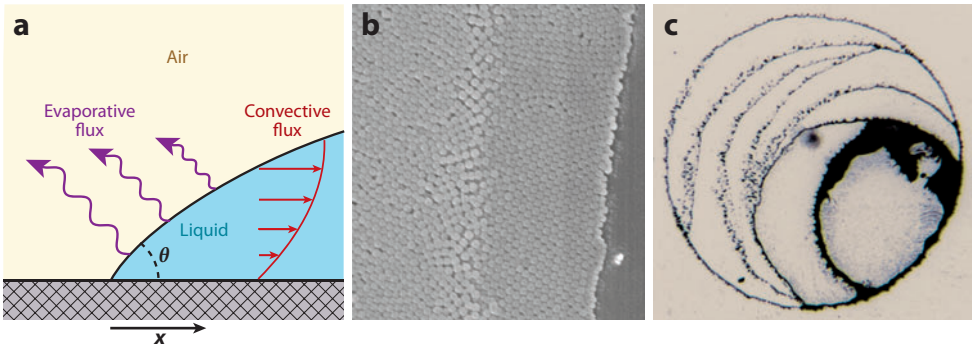

Figure 2

(*a*) The evaporative flux for a drop of volatile liquid, which is strongest near the contact line (Deegan et al. 1997). The mass transport inside the drop arises from competition between the evaporative flux (inducing mass flux to the left) and the receding velocity of the contact line (inducing mass flux to the right). The contact angle is indicated by θ, and x is the distance to the contact line. Panel *a* adapted from Berteloot et al. (2008). (*b*) Magnified image of a stripe pattern left by the moving contact line of a dilute suspension of silica spheres (diameter 123 nm). A multilayer close-packed array of particles can be observed. Panel *b* reprinted with permission from Watanabe et al. (2009). Copyright 2009 American Chemical Society. (*c*) Photograph of a solid surface after the evaporation of dilute suspension of TiO_2 nanoparticles in ethanol. Rings of accumulated particles correspond to the sticking phase of a stick-slip cycle. Panel *c* reprinted with permission from Moffat et al. (2009). Copyright 2009 American Chemical Society.

We first introduce the basic concepts of static and dynamic contact lines in Section 2, and Section 3 highlights the multiscale nature of the moving–contact line problem. We then extensively review experimental and theoretical work on dynamical wetting transitions in Section 4 and discuss the influence of molecular processes on contact line motion in Section 5. We close with a summary of the different regimes of contact line motion and list some future issues in Section 6.

2. STATIC VERSUS DYNAMIC CONTACT LINES

2.1. Basic Concepts

From a thermodynamic point of view, the molecular forces give rise to a surface tension defined as the Gibbs free energy per surface area of an interface separating two phases (de Gennes et al. 2002, Rowlinson & Widom 1982). Equivalently, from a mechanical point of view, surface tension is the resultant force per unit length due to a normal stress anisotropy in the vicinity of the interface (Kirkwood & Buff 1949). For curved interfaces, this gives rise to a pressure jump, also called the Laplace pressure. The equilibrium shape of a meniscus climbing a wall, or of a puddle of liquid on a surface, results from the balance between this surface tension γ and gravity g. The balance is governed by a characteristic length scale given by the capillary length $\ell_\gamma = \sqrt{\gamma/\rho g}$, which is typically 1 mm (with ρ the liquid density).

At the three-phase contact line, the wettability of the surface determines the equilibrium contact angle θ_e of the liquid on the solid. Minimization of the Gibbs free energy shows that θ_e is determined by a balance of solid-vapor, solid-liquid, and liquid-vapor surface tensions:

$$\cos\theta_e = \frac{\gamma_{SV} - \gamma_{SL}}{\gamma}, \qquad (1)$$

which is known as Young's (1805) law. Throughout, we use γ for the surface tension of a liquid-vapor (or liquid-gas) interface. In practice, even the cleanest surfaces are not perfectly

Laplace pressure: difference in pressure $\Delta p = \gamma\kappa$ across an interface of curvature κ, induced by capillary forces

Capillary length: length scale arising from the balance of surface tension and gravity, determining the rise of a static meniscus

homogeneous and exhibit chemical or geometrical heterogeneities (de Gennes 1985). This unavoidably leads to contact angle hysteresis, in which static contact angles can be achieved in the range $\theta_r < \theta < \theta_a$. Here $\theta_{a,r}$ are called advancing and receding contact angles, respectively. This emphasizes that the contact angle is selected at the molecular scale (Snoeijer & Andreotti 2008), and it therefore acts as a boundary condition for the macroscopic interface.

Contact angle hysteresis: even the cleanest substrates allow for a finite range of static contact angles, rather than a single equilibrium contact angle

2.2. The Singular Flow Geometry Near a Contact Line

The situation is completely different when the contact line moves with respect to the substrate, in which case the system is no longer at equilibrium. Even for an infinitesimal velocity U, the six decades separating the molecular size (nanometer scale) from the capillary length (millimeter scale) are the locus of a force absent from the static problem: viscosity. The hydrodynamics is in essence described by a corner flow (Huh & Scriven 1971), which has no intrinsic length scale (**Figure 3**). We can draw a few general conclusions from this. First, the lack of intrinsic length scale of the flow means that one can define only a local Reynolds number, based on the distance to the contact line r. As this distance can become arbitrarily small, the Reynolds number is typically very small, and inertia can often be neglected. Second, the viscous stress near the contact line scales as $\sim \eta U/r$, where η denotes the dynamical viscosity of the liquid. Hence the shear stress diverges upon approaching the contact line at $r = 0$. It is instructive to rephrase this in terms

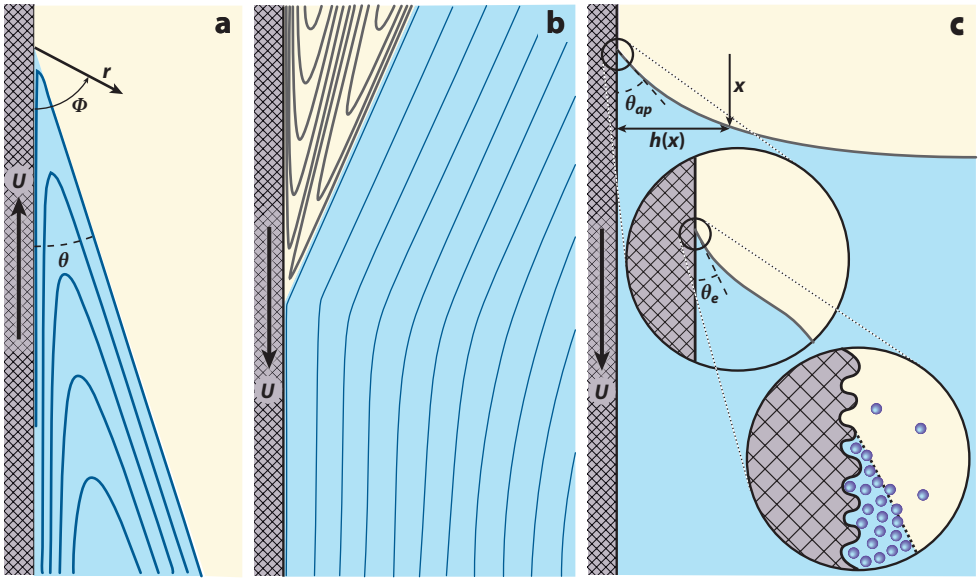

Figure 3

Streamlines in a wedge with planar interfaces (Huh & Scriven 1971) of angle θ for (*a*) a receding contact line (one-phase flow, with θ close to zero) and (*b*) an advancing contact line (two-phase flow, with θ close to π). In the advancing case, the viscous dissipation in the gas phase can dominate over the liquid phase because of the strongly confined circulation in the gas wedge. (*c*) Interface profile $h(x)$ for a plunging plate under partial wetting conditions. The interface near the contact line is highly curved so that the apparent contact angle θ_{ap} on the macroscopic scale is much larger than the true contact angle θ_e at the nanoscopic scale. The intermediate close-up represents the hydrodynamic regime governed by viscosity and surface tension. Panel *c* adapted from Bonn et al. (2009).

of the rate of energy dissipation $\dot{E}$ (per unit contact line), which between a distance r and $r + dr$ scales as (Bonn et al. 2009, de Gennes 1985)

$$d\dot{E} \sim \eta U^2 \frac{dr}{r} \sim \eta U^2 \, (d \ln r). \tag{2}$$

This implies that the total dissipation is not integrable at $r = 0$ nor at ∞, and one requires a cutoff at both small and large scales (Dussan & Davis 1974, Huh & Scriven 1971). Typically, these cutoffs appear at the molecular scale ($\sim 10^{-9}$ m) and at the scale of the capillary length ℓ_γ ($\sim 10^{-3}$ m). Each decade between the microscopic scale and the macroscopic scale contributes a comparable amount to the viscous dissipation, revealing the multiscale character of wetting flows.

Dip coating: common geometry to study wetting and coating, in which a solid surface is plunged into or withdrawn from a bath

These features of moving contact lines were first appreciated by Huh & Scriven (1971), who analytically solved the flow in a wedge assuming a perfectly planar liquid-vapor interface, using similarity solutions (**Figure 3**). The viscosity-dominated flow is described by Stokes equations, which in two dimensions can be reduced to the biharmonic equation $\nabla^4 \psi = 0$. Here $\psi(r, \phi)$ is the stream function expressed in polar coordinates (r, ϕ). Using a no-slip boundary condition at the wall, $u_r = -U$, one derives the similarity solution for flow in a corner, $\psi(r, \phi) = Ur(A \cos\phi + B \sin\phi + C\phi \cos\phi + D\phi \sin\phi)$. The coefficients are determined by the four boundary conditions: The solid is impermeable and allows no slip, whereas the free surface is impermeable and has no shear stress. The corresponding streamlines are sketched in **Figure 3** for one-phase and two-phase flows. The solutions by Huh & Scriven also reveal that there is a viscosity-induced pressure on the free surface. This pressure must be balanced by the capillary pressure and hence requires a curvature of the interface. In this sense, the wedge with a planar liquid-vapor interface is not a full solution of the moving–contact line problem: The free surface will be strongly curved close to the contact line (Dussan 1979). The dimensionless number that describes this viscocapillary balance is the capillary number,

$$\mathrm{Ca} = \frac{U\eta}{\gamma}, \tag{3}$$

which is the key parameter for moving contact lines.

3. COUPLING OF MOLECULAR AND MACROSCOPIC SCALES

The interplay between the different length scales is illustrated using the paradigmatic example of dip coating, which has obvious importance in coating applications. As sketched in **Figure 3*c***, a

EVAPORATION

A similar corner singularity is encountered when liquid drops evaporate on a surface (**Figure 2**) (Deegan et al. 1997). When evaporation is controlled by vapor diffusion and for small contact angles, the evaporative flux diverges as $j = J_0/\sqrt{x}$, where x is the distance to the contact line and J_0 is a constant. Inside the liquid, this induces a flow $U_{evap} \sim J_0/\theta\sqrt{x}$, oriented toward the contact line. Interestingly, an evaporative contact line usually recedes over the substrate, in the direction opposite to U_{evap} (Cazabat & Guena 2010). Comparing the receding velocity U with U_{evap}, one obtains a length scale $\ell_{evap} = (J_0/\theta U)^2$ that can be as large as 100 μm (Berteloot et al. 2008). This length separates regions where mass transport is toward or directed away from the contact line (**Figure 2*a***). When the liquid contains colloidal particles or polymers, the evaporation leads to self-assembly and pattern formation (Abkarian 2004). A well-known example is provided by the dark edge of a coffee stain, consisting of particles transported by U_{evap}. **Figure 2*c*** shows a case in which this has induced a stick-slip motion of the contact line, leaving various deposits.

partially wetting solid substrate is plunged into a liquid reservoir at a velocity U. The successive close-ups near the contact line illustrate the physics at different scales. On the macroscopic scale of the capillary length ℓ_γ, the shape of the meniscus is governed by the balance of gravity and surface tension; at smaller scales, one encounters a viscocapillary regime characterized by the capillary number Ca. This section addresses the physics of these regimes and how they are coupled. The ultimate close-up in **Figure 3*c*** is on the molecular scale, which we treat separately in Section 5.

3.1. Macroscopic Scales: Apparent Contact Angle

When plunging the plate at moderate velocities, the meniscus attains a steady shape in the frame of the reservoir. **Figure 4*a*** shows experimental measurements of the meniscus shape by Ramé & Garoff (1996). The lower data set is the shape at Ca $= 0$, which is accurately fitted by the analytical

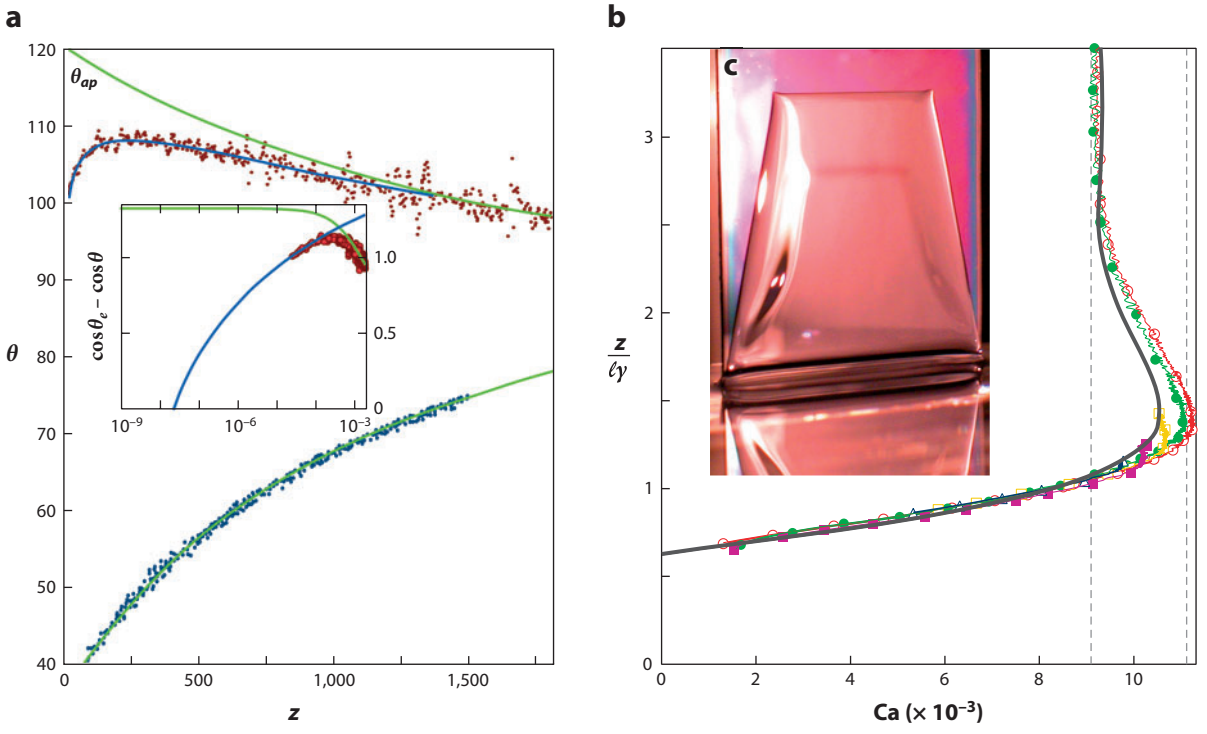

Figure 4

(*a*) Shape of a dynamic interface measured by Ramé & Garoff (1996) for a cylinder plunged in a bath of silicon oil ($\theta_e \sim 35°$). The dots represent the local angle of the meniscus with respect to the substrate, θ, as a function of the horizontal distance to the contact line: (*blue dots*) static meniscus, Ca $= 0$, and (*red dots*) dynamical meniscus, Ca $= 0.1$. The green solid lines are the analytical solutions for an equilibrium profile. (*Inset*) Same data on a logarithmic scale. The blue solid line is the hydrodynamic prediction in the viscocapillary regime. Experimental points do not reach below distances of approximately 10 μm from the contact line, but the interface is curved down to nanometer scales. The green line is the fit of the macroscopic shape of the interface ($\theta \to 90°$ at the bath) by the static solution. Extrapolation to 120° defines the apparent contact angle θ_{ap}. Data taken from Ramé & Garoff (1996). (*b*) Partially wetting plate withdrawn from a silicon oil bath at capillary number Ca, forming a dynamic contact line at height z (Ca). The thick gray line is derived from the multiscale lubrication theory. The colored data sets correspond to different experimental realizations. The maximum capillary number is reached close to $z_c = \sqrt{2}\ell_\gamma$, which corresponds to $\theta_{ap} = 0$. Data taken from Delon et al. (2008). (*c*) A liquid film is entrained above the critical capillary number Ca_c. The film consists of two parts of incompatible thickness joined by a shock. Panel *c* adapted with permission from Snoeijer et al. (2006). Copyright 2006 by the American Physical Society.

solution for an equilibrium profile. The upper data set is the dynamical meniscus shape at Ca = 0.1. Here the variation of the angle θ is nonmonotonic: It first increases with distance to the contact line, whereas it decreases to connect to the bath at 90°. Again the large-scale solution can be accurately fitted by the formula for a static meniscus solution. On smaller scales, one observes the onset of the viscosity-dominated hydrodynamic regime (Kavehpour et al. 2003, Ramé & Garoff 1996).

Extrapolating the static outer solution toward the contact line leads to an apparent macroscopic contact angle θ_{ap}, which in this case is approximately 120°. A simple way to extract θ_{ap} from the experiment is to measure the elevation of the contact line over the bath, z, using the static meniscus solution (Landau & Lifshitz 1984):

$$z = \ell_\gamma \sqrt{2(1 - \sin\theta_{ap})}. \tag{4}$$

Clearly, the apparent contact angle of a meniscus depends on Ca, as it determines how far the system is pushed from equilibrium. For advancing contact lines θ_{ap} is greater than θ_e (as in **Figure 4*a***), whereas $\theta_{ap} < \theta_e$ in the receding case. In many flow situations, where Ca is small, the apparent contact angle completely describes the dynamics. Examples are drop spreading (Hocking 1983), drops sliding down a window at low velocities (Ben Amar et al. 2003, Rio et al. 2005), and the relaxation of contact line perturbations (Golestanian & Raphaël 2001, Nikolayev & Beysens 2003, Snoeijer et al. 2007b).

Apparent contact angle: an extrapolated angle based on the large-scale meniscus profile (not the true angle of the interface)

Lubrication approximation: systematic method to simplify the hydrodynamic equations, which is valid for a quasi-parallel flow (for small contact angles)

Viscous bending: viscosity-induced curvature of the interface, with a local contact angle that varies logarithmically with the distance to the contact line

3.2. Mesoscopic Scales: Hydrodynamic Regime

We now turn to a detailed description of the hydrodynamic regime. This refers to the distances to the contact line that are smaller than the capillary length, at which the meniscus shape is influenced by viscous effects.

3.2.1. The viscocapillary balance. The balance between viscosity and surface tension is most easily captured using the lubrication approximation, for which the angles are assumed small (Oron et al. 1997). The Stokes flow then reduces to a third-order differential equation for the interface profile $h(x)$, as defined in **Figure 3*c***,

$$\frac{d^3h}{dx^3} = -\frac{\sigma\, 3\mathrm{Ca}}{h^2}, \tag{5}$$

which expresses the balance between the capillary and the viscous stresses. Here σ is $+1$ for advancing contact lines and -1 for receding contact lines. With this convention, Ca is considered positive for both advancing and receding cases.

3.2.2. The Voinov solution. Remarkably, the highly nonlinear Equation 5 has an exact solution (Duffy & Wilson 1997). In some specific asymptotic limits, the exact solution reduces to the form proposed by Voinov (1976),

$$h'(x) \approx \theta(x) \simeq [9\,\mathrm{Ca}\ln(x/c)]^{1/3}. \tag{6}$$

This relation reveals the viscous bending of the interface: The contact angle varies logarithmically with the distance to the contact line. This asymptotic solution by Voinov is valid up to large distances $x \to \infty$ for advancing contact lines ($\sigma = 1$ in Equation 5) but not for receding contact lines ($\sigma = -1$). The solution has the convenient property that the macroscopic curvature $h''(\infty)$ is zero, which can thus be imposed as a macroscopic matching condition for advancing contact

lines. For receding contact lines, the matching to macroscopic scales is more intricate (Eggers 2004, 2005b).

Matching: term borrowed from matched asymptotic expansion; often loosely used to indicate the coupling of solutions at different scales

Equation 6 can be generalized to flows with large contact angles, i.e., beyond the assumptions of the lubrication approximation (Cox 1986, Snoeijer 2006, Voinov 1976), by a perturbation expansion around the Huh & Scriven solutions. Surprisingly, the generalized result for $\theta(x)$ is almost identical to Equation 6, to within a few percent, up to angles as large as 150°. This means that Equation 6 is applicable to the experimental data for $\theta(x)$ shown in **Figure 4**. Indeed, the Voinov solution accurately describes the onset of the viscous regime and bridges the gap between molecular and macroscopic scales.

3.3. Matching

The matching of the equilibrium solution to the mesoscopic/hydrodynamic solution provides the relation between θ_{ap} and Ca (Cox 1986, Hocking 1983, Voinov 1976). In cases in which Equation 6 represents the correct asymptotics, the matching reduces to the Cox-Voinov law

$$\theta_{ap}^3 = \theta_e^3 + 9\sigma\,\mathrm{Ca}\ln\left(\frac{\alpha\ell_o}{\ell_i}\right). \tag{7}$$

Here ℓ_o is an outer (macroscopic) length (i.e., the capillary length or the size of a spreading drop), whereas ℓ_i is an inner (microscopic) length that represents the molecular processes that regularize the viscous singularity (which relates to c in Equation 6). The numerical constant α is nonuniversal and depends on details of the microscopic and macroscopic boundary conditions (Cox 1986, Eggers & Stone 2004).

We emphasize that Equations 6 and 7 correspond to a particular solution of the hydrodynamic problem, and hence they are not universally applicable. A prime example that is not described by the Cox-Voinov relation is dip coating with a reversed plate velocity, i.e., where the plate is withdrawn from the bath (Eggers 2004, 2005b). In this case, Equation 5 does not admit any solutions with $h''(\infty) = 0$, and the matching requires the full analytical solution by Duffy & Wilson (1997). **Figure 4*b*** shows the bifurcation diagram for steady-state solutions for plate withdrawal (Delon et al. 2008, Snoeijer et al. 2007b). The menisci are represented by the meniscus rise z, related to θ_{ap} according to Equation 4, for various plate velocities Ca. The maximum possible plate velocity, or critical capillary number Ca_c, is typically of the order of 0.01, or even less for small contact angles. The critical speed is achieved at $z_c \approx \ell_\gamma\sqrt{2}$. This means that at the maximum speed, the apparent contact angle vanishes, $\theta_{ap} \approx 0$ (Chan et al. 2011, Maleki et al. 2007, Sedev & Petrov 1991, Snoeijer et al. 2007b), consistent with the conjecture by Deryaguin & Levi (1964) and with the matched asymptotic expansion by Eggers (2004). Interestingly, the steady-state solutions continue beyond this critical meniscus rise, on to a higher branch of meniscus solutions. It is impossible to attribute an apparent contact angle to these meniscus shapes based on Equation 4 (Chan et al. 2012).

Figure 4*b* illustrates that the menisci for plate withdrawal are governed by a nontrivial bifurcation scenario, which is predicted by hydrodynamics, but which reaches beyond a simple picture based on an apparent contact angle. How quantitative is the hydrodynamic prediction, e.g., for the critical speed Ca_c? The lubrication model leading to the solid line in **Figure 4*b*** accounts only for the viscous dissipation between the microscopic scale, here characterized by a slip length of two molecular sizes, and the capillary length. The microscopic contact angle was assumed equal to the receding equilibrium angle θ_r. We emphasize that the hydrodynamic prediction is quite sensitive to the microscopic contact angle, as can be expected for small Ca: The few degrees of uncertainty related to contact angle hysteresis induce variations of the critical Ca_c by as much as

20%. This is the level of quantitative agreement typically achieved by the hydrodynamic theory. The precise value of the slip length only weakly (logarithmically) affects the results. We return to this important point in Section 5 in which we review molecular process in detail. However, as any other source of dissipation would add up to viscous dissipation, this quantitative agreement with experiments suggests that most of the dissipation takes place in the hydrodynamic scales (roughly from 10 nm to 1 mm).

4. DYNAMICAL WETTING TRANSITIONS

An interesting situation arises when a liquid is forced to flow over a surface that it does not spontaneously wet in thermodynamic equilibrium. In such partial wetting conditions, it is energetically favorable for the liquid to leave most of the surface dry. However, an external driving of the flow can push the system sufficiently far from equilibrium such that it undergoes a dynamical wetting transition. In practical terms, this means that the contact line motion cannot exceed a maximum speed: Enforcing larger velocities leads, for example, to the deposition of liquid films, breakup of liquid drops, or entrainment of air bubbles. In this section we summarize recent experimental and theoretical progress on the nature of these dynamical wetting transitions.

4.1. Entrainment of Liquid Films

One of the simplest ways to deposit a thin film of liquid is by withdrawing a solid from a reservoir (**Figure 4*b***) such that the contact line is receding. Under complete wetting conditions, this dip coating gives a uniform film of thickness that is controlled by the speed of withdrawal. This goes back to the pioneering work by Landau & Levich (1942) and Deryaguin (1943), who demonstrated that the thickness $h_{LLD} \sim \ell_\gamma \mathrm{Ca}^{2/3}$.

The situation is much more complex when the liquid is partially wetting the solid. **Figure 4*b*** shows that the contact line can rise to a steady position without leaving a film when the speed of withdrawal is sufficiently small (Snoeijer et al. 2007b). Above a critical Ca_c, however, steady-state solutions cease to exist, and a dynamical wetting transition occurs (Blake & Ruschak 1979, Eggers 2004, Quéré 1991, Sedev & Petrov 1991, Snoeijer et al. 2006). The physics of this dynamical wetting transition is such that above the critical speed, the capillary forces can no longer compete with the large viscous forces that develop inside the flow (de Gennes 1985).

Above the critical speed, one observes the dynamical evolution of a liquid film that is very different from the smooth Landau-Levich film (**Figure 4*c***). The dynamical film solution splits into two parts because of a mismatch of microscopic and macroscopic boundary conditions (Snoeijer et al. 2006). Immediately behind the contact line, there is a thick film of thickness h_f, which is determined by the microscopic boundary conditions imposed at the contact line. At the side of the reservoir, one observes the Landau-Levich-Derjaguin film. The two solutions are connected by a shock that travels upward with respect to the reservoir, at a velocity described accurately by lubrication theory (Snoeijer et al. 2006). In terms of the capillary number, the thickness in front of the shock scales as $h_f \sim \ell_\gamma \mathrm{Ca}^{1/2}$, which at small Ca is indeed thicker than $h_{LLD} \sim \ell_\gamma \mathrm{Ca}^{2/3}$.

4.2. V-Shaped Contact Lines

Stability analysis has shown that an infinitely extended, straight contact line is linearly stable for all capillary numbers, all the way up to the critical point (Golestanian & Raphaël 2001, Snoeijer et al. 2007b). Experimentally, however, the finite lateral extension of the contact line has major practical consequences. This can be seen in **Figure 4*c***: No entrainment occurs at the sharp edge

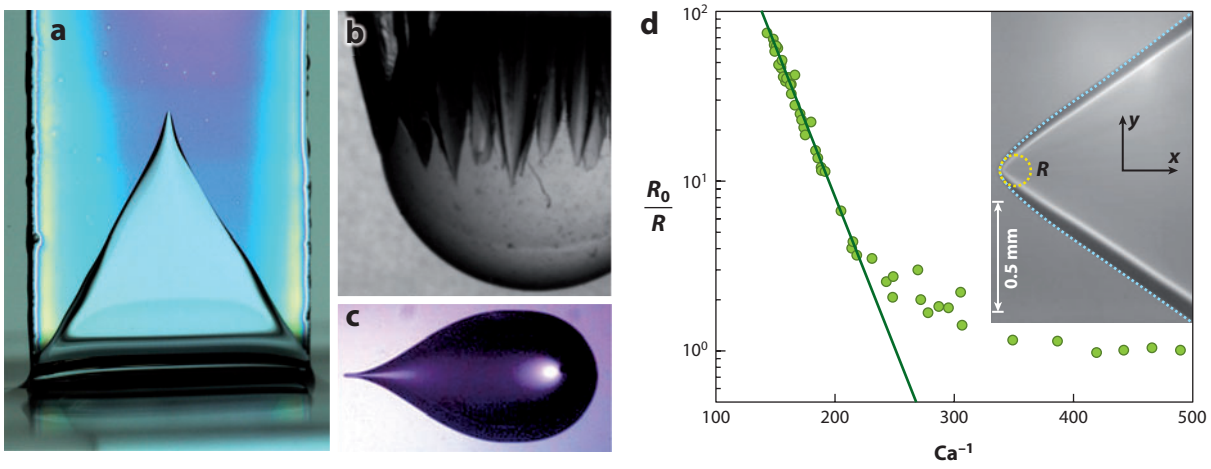

Figure 5

V-shapes appearing at the dynamical wetting transition: (*a*) dip coating (Delon et al. 2008); (*b*) sphere plunging in a bath, as in **Figure 1** (Duez et al. 2007); (*c*) silicon oil drop moving down an inclined plane (Podgorski et al. 2001); and (*d*) radius of curvature R of the rounded edge of a cornered drop as a function of Ca. The solid green line is the prediction by hydrodynamic theory. Panel *a* adapted from Delon et al. (2008), reproduced with permission from Cambridge University Press. Panel *b* courtesy of Lyderic Bocquet and panel *c* courtesy of Laurent Limat.

of the wafer, inducing a sharp kink in the contact line higher up the solid. Indeed, such corners, or V-shapes, are a generic feature of advancing and receding contact lines near a transition.

4.2.1. Reducing the contact line normal speed. **Figure 5** represents a broad collection of contact lines that spontaneously develop a V-shape (Blake & Ruschak 1979, Delon et al. 2008, Duez et al. 2007, Le Grand et al. 2005, Peters et al. 2009, Podgorski et al. 2001, Winkels et al. 2011). In all experiments, the corners start to emit little droplets (receding contact lines) or bubbles (advancing contact lines) when moving at even higher speeds. Note that advancing corners appear at much higher velocities than receding corners. The ratio of advancing to receding speeds is about 10 for water (Duez et al. 2007, Podgorski et al. 2001) but can be even larger than 100 for very viscous liquids (Benkreira & Khan 2008).

The formation of a corner is an elegant way to delay the dynamical wetting transition. The physical mechanism, first described by Blake & Ruschak (1979), is that the inclination of the contact line reduces the normal velocity, $U_\perp \sim U \sin\phi$. Here ϕ is the top-view angle of the corner. As the local fluid velocity near the contact line is equal to $U_\perp$ (Rio et al. 2005), the effective driving is reduced by a factor $\sin\phi$. In analogy to the Mach cone for supersonic flows, it was proposed that the top-view angle evolves according to $\sin\phi \sim U_c/U$ to maintain a normal velocity below the critical speed U_c (Blake & Ruschak 1979, Podgorski et al. 2001). Although this argument provides a good description for large top-view angles, it does not capture the pearling transition, i.e., the dynamical wetting transition at which small droplets are emitted from the corner tip (Snoeijer et al. 2007a).

4.2.2. The case of sliding drops. The dewetting corners appearing at the rear of sliding drops can be understood from a model that considers the tip of the corner to be infinitely sharp. By assuming a perfect conical geometry of the interface, Limat & Stone (2004) identified a similarity solution that describes the three-dimensional shape of the interface. Defining the coordinates (x, y) as in **Figure 5*d***, these solutions are of the form $h(x, y) = x\Omega\,\mathrm{Ca}^{1/3}\mathcal{H}(y/x)$, where Ω is the

side-view angle and $\mathcal{H}$ is the cross-sectional similarity profile of the cone. The cone solution has a vanishing interface curvature along the central axis in the direction of the flow, i.e., $\partial^2 h/\partial x^2 = 0$. This is fundamentally different from straight contact lines because, for the corners, the side-view angle $\partial h/\partial x = \Omega$ no longer varies with x. Instead, the driving capillary forces inside a corner originate from the transverse curvature, $\partial^2 h/\partial y^2 \sim \mathrm{Ca}^{1/3}/x$. This three-dimensional feature is not captured by the Mach-cone argument and is crucial for explaining the pearling transition (Snoeijer et al. 2007a).

The fine structure of the corner tip can be characterized by the curvature $1/R$ of the contact line. **Figure 5*d*** shows the tip curvature for different speeds before the pearling transition (Peters et al. 2009). Whereas at small velocities $1/R$ is approximately constant, the tip curvature increases dramatically near the transition. This can be understood quantitatively from a variation of the Cox-Voinov relation (Equation 7). At a small distance from the tip (much smaller than R), the contact line is effectively straight. In this regime, one expects the usual contact line dynamics characterized by an inner microscopic scale ℓ_i. The behavior changes at distances of order R, at which the geometry becomes truly three dimensional and the transverse curvature provides the dominant capillary driving force. Interpreting Equation 7 as an equation for R, one obtains

$$R = \alpha^{-1}\ell_i \ \exp\left(\frac{\theta_e^3 - \theta_{ap}^3}{9\mathrm{Ca}}\right) \approx \alpha^{-1}\ell_i \ \exp\left(\frac{\theta_e^3}{9\mathrm{Ca}}\right). \qquad (8)$$

This relation is shown as the prediction by hydrodynamic theory in **Figure 5*d***. It accurately describes the experimental data, upon fitting a microscopic length $\alpha^{-1}\ell_i = 7$ nm.

4.3. Dewetting Holes

Another class of dewetting transitions is encountered after a partially wetting surface is covered by a macroscopic liquid film. Thermodynamically, such a film is metastable because the surface free energy can be reduced by collecting the film into liquid drops. There are two mechanisms that lead to such dewetting. The first is encountered when the thickness falls within the range of microscopic interactions (typically 2–10 nm). This induces a linear instability (spinodal dewetting) that is characterized by a well-defined wavelength (Reiter 1992, Saulnier et al. 2002, Seemann et al. 2001, Thiele 2003). A second mechanism is induced by large-amplitude perturbations: Once a small hole is nucleated inside the film and a contact line appears, the hole will rapidly grow and dewet the surface (Brochard-Wyart et al. 1987, de Gennes et al. 2002, Redon et al. 1991). Here we consider the second mechanism, which involves a moving contact line. **Figure 6** shows a snapshot of a hole for the dewetting of an air film (**Figure 6*a***) and for a liquid film (**Figure 6*b***). As the contact line bordering the film retracts over the solid, the liquid or air inside the film is collected into a rim, which grows slowly in time. It is found experimentally that the speed of retraction of a viscous film is constant (Redon et al. 1991).

The problem consists essentially of a receding front at the contact line forming the front of the rim, coupled to an advancing front forming the back of the rim. The dewetting speed is determined by equating θ_{ap} for the advancing front to θ_{ap} of the receding front (de Gennes et al. 2002). This viewpoint was confirmed recently by matched asymptotic expansion of the lubrication equations (Flitton & King 2004, Snoeijer & Eggers 2010). The receding front shown in **Figure 6*d*** represents an exact solution of Equation 5, which is matched to the advancing front. As a result, it was found that the appropriate law for $\theta_{ap}(\mathrm{Ca})$ was not the classical result by de Gennes (1986), as was previously assumed (de Gennes et al. 2002), but was instead the Cox-Voinov relation. The advancing front is described by Equation 7, with $\theta_e = 0$, and involves the rim width w and

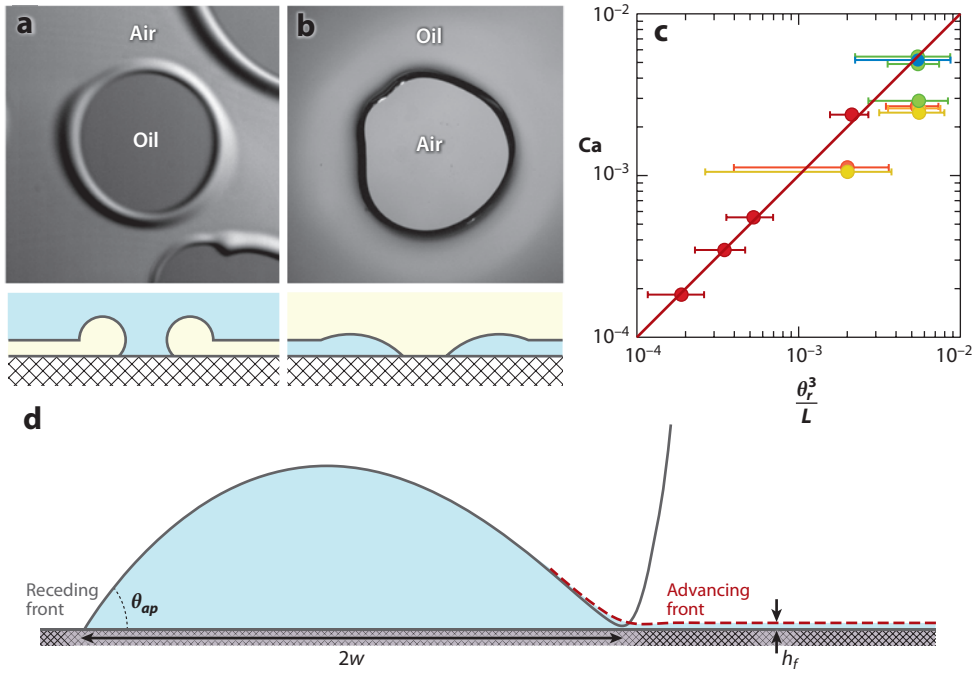

Figure 6

Dewetting holes. (*a*) Image and schematic of a rewetting hole observed when a film of air is entrained dynamically into a silicon oil bath. (*b*) Image and schematic of a dewetting hole observed for a film of silicon oil on a fluorinated substrate. (*c*) Dewetting capillary number as a function of the receding contact angle θ_r. L is the logarithmic factor appearing in Equation 9. Different colors represent different molecular weights of the liquid. The error bars mainly reflect the uncertainty on the contact angle. Panel *c* data taken from Redon et al. (1991). The solid line corresponds to the hydrodynamic theory (Equation 9). (*d*) Cross section of the solution obtained by asymptotic matching of the receding front (*gray solid line*) and the advancing front (*dashed red line*). Panel *d* adapted from Snoeijer & Eggers (2010).

film thickness h_f as relevant length scales. The receding contact line ($\sigma = -1$) involves a ratio w/ℓ_s, where ℓ_s is the slip length. Equating the advancing and receding θ_{ap}, Snoeijer & Eggers (2010) found the velocity

$$\mathrm{Ca} = \frac{\theta_e^3}{9}\left[\ln\left(\frac{4a\theta_e \mathrm{Ca}^{1/3}}{3e}\frac{w^2}{\ell_s h_f}\right)\right]^{-1}, \qquad (9)$$

where a is the numerical constant $a = 1.094\ldots$. **Figure 6*c*** replots the dewetting speeds for different liquids and wettabilities obtained by Redon et al. (1991). Here the factor L represents the logarithmic factor in Equation 9, in which the slip length ℓ_s was estimated as $2\sqrt{N}a$, where the N is the number of monomers and a the monomer size (see Section 5.1). All experimental data are consistent with the hydrodynamic prediction of Equation 9.

4.4. Entrainment of Air

The dynamical wetting transition for advancing contact lines results in the entrainment of air. The splash in **Figure 1** arises when the contact line cannot advance sufficiently fast over the solid

to close the cavity in the wake of the sphere (Duez et al. 2007). Once again, the entrainment of air occurs at much larger speeds than the dynamical wetting transition for receding contact lines. Typical values for the critical Ca are of order 1 for advancing contact lines (Benkreira & Khan 2008, Marchand et al. 2012) instead of 0.01 as observed for receding contact lines. For very hydrophobic surfaces, the splashing threshold scales as $\mathrm{Ca} \sim (\pi - \theta_e)^3$ (**Figure 1*a***). This is strongly reminiscent of the θ_e^3 dependence characteristic for receding contact lines (see, e.g., Equation 9). This suggests that the critical speed is governed by the gas phase, which consists of a wedge of angle $\pi - \theta_e$ and which is receding over the solid (**Figure 3*b***). A similar dependency on θ_e was found for drop emission by liquid filaments and in simulations (Do-Quang & Amberg 2009, Ledesma-Aguilar et al. 2011).

The mutual influence of the liquid and gas phases on air entrainment was mostly investigated in the context of dip coating (Benkreira & Ikin 2010, Benkreira & Khan 2008, Blake & Ruschak 1979, Burley & Kennedy 1976, Marchand et al. 2012, Simpkins & Kuck 2000). These experiments typically vary the dynamical viscosity of the liquid phase η: The critical speed decreases for more viscous liquids, suggesting that dissipation in the liquid is important. However, the dependence is much less than the expected $\sim 1/\eta$. Marchand et al. (2012) showed that this can be attributed to the gas viscosity: The dissipation in the air becomes significant because of the confinement of the wedge of air (**Figure 3*b***). Another striking effect is that the critical speed increases when the air pressure is reduced to approximately 1–10% atm. Because such a pressure change does not affect the gas viscosity, this effect must result from inertia in the gas or from the increase of the mean free path. The latter would imply a larger slip length, which reduces the dissipation in the gas and leads to a larger critical speed (Marchand et al. 2012). Similar effects of the gas phase were observed in drop splashing (De Ruiter et al. 2012, Mandre et al. 2009, Tsai et al. 2010, Xu et al. 2005). A definitive description of the role of the air in dip coating and in splashing is still lacking.

5. MOLECULAR PROCESSES

An important conclusion reached in nanofluidics is that the Navier-Stokes equations remain valid down to the nanometer scale for simple fluids such as water under normal conditions (Bocquet & Charlaix 2010). This means that from ~10 nm from the contact line up to macroscopic scales, the shape of a moving interface can be described by continuum hydrodynamics. In this section, we review different processes that become relevant at the scale at which hydrodynamics breaks down. We anticipate that all descriptions require two physical quantities: (*a*) a length scale that measures at what scale microscopic processes start to play a role and (*b*) an energy scale that expresses the strength of the interaction with the solid (i.e., the wettability). We first concentrate on mechanisms that are commonly used in combination with continuum hydrodynamics, for example, in the context of numerical simulations involving moving contact lines (Section 5.1). We then turn to thermally activated processes (Section 5.2), for which we point out similarities and differences with the hydrodynamic theory.

5.1. Slip Length, Disjoining Pressure, and Diffuse Interface Models

Any description of wetting hydrodynamics requires a microscopic model to release the moving–contact line singularity. Here we discuss three different physical mechanisms, namely slip, molecular interactions, and diffusion, and comment on how these affect the motion of contact lines.

5.1.1. Slip length. It is now well established that motion of the first few molecular layers above a solid substrate can be described by the Navier slip boundary condition:

$$u_{z=0} = \ell_s \frac{\partial u}{\partial z}, \tag{10}$$

where ℓ_s is called the slip length, and $z = 0$ denotes the position of the wall. For gases, the existence of velocity slip was first predicted by Maxwell (1878), who argued that the slip length must be proportional to the mean free path ℓ_{mfp}. This proportionality $\ell_s \sim \ell_{mfp}$ was demonstrated experimentally (Andrew & Harris 1995), numerically (Morris et al. 1992), and analytically (Bocquet 1993), with a proportionality constant of 2.4 in experiments. For liquids, a fully microscopic prediction for the slip length was derived from the statistical physical theory of liquids (Huang et al. 2008):

$$\ell_s \sim \frac{\eta D a \; k_B T}{[\gamma a^2 (1 + \cos\theta_e)]^2} a. \tag{11}$$

This expression contains the molecular size a, the self-diffusion coefficient D, and a wettability factor $\gamma(1 + \cos\theta_e)$ that arises from the tangential forces on the liquid near the wall. Indeed, the dependence $(1 + \cos\theta_e)^{-2}$ is approximately verified in experiments and in numerical simulations (Bocquet & Charlaix 2010, Huang et al. 2008). Moreover, for simple liquids, the Stokes-Einstein relation is approximately valid and leads to $\eta D a \sim k_B T$. As a consequence, the slip length ℓ_s is not expected to depend on the liquid viscosity for simple liquids. Polymer solutions typically exhibit much larger slip lengths of the order of the molecule size, $2\sqrt{N}\,a$, where N is the number of monomers and a the monomer size.

5.1.2. Slip and moving contact lines. For moving contact lines, the Navier slip condition leads to a regularization of the viscous stress divergence discussed in Section 2.2 (Dussan & Davis 1974). In the lubrication approximation, the viscous stress applied to the solid by a flowing film of thickness h is $3\eta U/(h + 3\ell_s)$, and the rate of dissipation per unit contact line becomes

$$\dot{E} = \frac{1}{2}\eta U^2 \int \frac{3h}{(h + 3\ell_s)^2} dx. \tag{12}$$

This is now a convergent integral as the layer thickness $h \to 0$.

The Navier slip boundary condition is a popular treatment to remove the moving–contact line singularity: It is well established experimentally and theoretically, and it is easily incorporated into a continuum description. However, we wish to point out a couple limitations of the method. The main problem is that the slip condition introduces only a length scale, and not an energy scale, to express the interaction with the solid wall. In practice, this means that the hydrodynamic equations still lack a boundary condition for the microscopic contact angle, which is necessary to close the problem. Moreover, the introduction of slip regularizes the divergence of shear stress and energy dissipation, but it still leads to a logarithmically divergent pressure $p \sim \eta U/\ell_s \ln(h/\ell_s)$ (Buckingham et al. 2003).

5.1.3. Disjoining pressure. This interaction with the solid substrate can be introduced using an effective interface potential (de Feijter 1988). A common approximation is to write the interfacial free-energy functional (per unit contact line) as

$$\mathcal{F}[h(x)] = \int dx[\gamma(\sqrt{1 + h'^2}) + \omega(h)]. \tag{13}$$

The first term represents the capillary energy of the liquid-vapor interface, whereas $\omega(h)$ is an effective potential due to the finite thickness of the layer h. Taking the functional derivative of

Equation 13, one obtains the pressure discontinuity across the interface, $\delta\mathcal{F}/\delta h(x) = -\gamma\kappa + \Pi(h)$. The first term is the Laplace pressure due to interface curvature κ. The second is the disjoining pressure (or internal energy per unit volume), defined as $\Pi(h) = d\omega/dh$. Descriptions beyond Equation 13 lead to more complex nonlocal equations for the capillary pressure (Getta & Dietrich 1998, Merchant & Keller 1992, Snoeijer & Andreotti 2008).

By itself, the introduction of a disjoining pressure does not remove the contact line singularity (Dussan & Davis 1974). However, a common treatment involving a disjoining pressure is the introduction of a functional form for $\omega(h)$ that exhibits a minimum $\omega'(h = h^*) = 0$. Then the liquid interface tends to a precursor film of thickness h^*, for which the disjoining pressure $\Pi(h^*) = 0$ (Eggers 2005a, Pismen 2001, Pismen & Eggers 2008, Pismen & Pomeau 2000, Schwartz et al. 2005, Thiele et al. 2002). This method has the convenient property that it leads both to a selection of the microscopic contact angle and to regularization of the viscous stress because the liquid thickness is always nonzero, even without explicitly using the Navier boundary condition. The introduction of such a disjoining pressure avoids the caveats of the slip model. From a physical perspective, the drawback is that precursor films are usually not encountered under partially wetting conditions. It has been argued, however, that it is possible to include a $\Pi(h)$ that does not lead to precursor films (Colinet & Rednikov 2011, de Gennes et al. 1990).

5.1.4. Diffuse interface models. Above we implicitly assumed that the liquid-vapor interface is characterized by a mathematically sharp profile $h(x)$. One should bear in mind that the interface has a finite width, typically a few molecular sizes (Rowlinson & Widom 1982). This can be characterized by a variation in the (coarse-grained) density field $\phi(\vec{r})$, which smoothly connects the high-density liquid phase to the low-density vapor phase. The jump in density occurs over a scale ζ, the interface width. From the perspective of continuum hydrodynamics, the capillary forces inside the diffuse interface are described by a force per unit volume $\sim \nabla\phi$, which has to be incorporated in the Navier-Stokes equation (Jacqmin 2000; Qian et al. 2004, 2006; Yue & Feng 2011).

The diffuse interface framework is popular for numerical simulations, in particular when the flow geometry does not allow for a lubrication approximation. Even if the no-slip boundary condition is applied, the contact line can move through phase transition (for a liquid-vapor interface) or by diffusion (for two immiscible liquids). The characteristic length scale over which the phase transformation or diffusion occurs is determined by the diffusion length ℓ_D, which is a priori independent from the interface width ζ (Qian et al. 2006, Ren & E 2007). If a Navier slip boundary condition is imposed, the effective slip observed on a macroscopic scale is determined by the larger of the two lengths ℓ_s or ℓ_D. In addition, generalizations of the Navier slip boundary conditions have been proposed to account for the stresses inside the diffuse interface (Carlson et al. 2009, Qian et al. 2006, Ren & E 2007). In the simplest version, slip velocity is dominated by the unbalanced Young stress, leading to a law for the microscopic contact angle:

$$\cos\theta - \cos\theta_e \sim \mathrm{Ca}\frac{\zeta}{\ell_s}. \tag{14}$$

Note that for typical fluids, the lengths ζ, ℓ_D, and ℓ_s are expected to be of comparable magnitude.

5.2. Thermally Activated Processes

Thermal activation: motion toward a lower energy state across an energy barrier, induced by a rare thermal fluctuation

A rather different perspective on the dynamics of wetting is to consider that contact line motion is a thermally activated process (Blake 2006, Blake & De Coninck 2011, Blake & Haynes 1969, Seveno et al. 2009). The key idea of this molecular kinetic theory (MKT) is that a contact line

moves by small jumps induced by thermal fluctuations. Indeed, thermal noise leads to a stochastic stress inside the liquid that can compete with viscous and capillary stresses. For example, the thermal length $\ell_T = \sqrt{k_B T/\gamma}$ is the scale below which thermal activation can dominate capillary forces, inducing a roughening of the surface (Flekkoy & Rothman 1996). At room temperature, this thermal length is typically a few angstroms.

Below we first discuss the original interpretation of MKT, in which the size of elementary jumps is determined by the molecular structure of the liquid and of the nearly homogeneous substrate. In this case, the jump size is comparable to the thermal length ℓ_T, and we point out the relation to Eyring's model for viscosity. We then consider MKT as a description of contact lines moving on heterogeneous substrates. This corresponds to the limit in which the size of elementary jumps is much larger than the thermal length, and in which case MKT provides a detailed perspective on contact angle hysteresis.

5.2.1. Molecular kinetic theory for contact line motion. A full derivation of contact line hydrodynamics including thermal fluctuations has not yet been attempted. However, MKT provides a phenomenological description that treats contact line motion as a single mode of propagation, characterized by a length scale ξ and by an energy barrier for the activated process E^* (Blake 2006). On (nearly) homogeneous substrates, the activation length ξ is subnanometric (Seveno 2010), and the energy barrier is of the order of the solid-liquid interaction, $E^* \sim \gamma\xi^2(1+\cos\theta_e)$. Using the reaction rate theory for thermal activation (Hanggi et al. 1990), the frequency at which the barrier is crossed is $\nu = \nu_0 \exp(-\frac{E^*}{k_B T})$, where ν_0 is the attempt frequency. For molecular motion, the attempt frequency is typically the thermal frequency $\nu_0 \sim k_B T/h \sim 10^{13}$ Hz, where h is Planck's constant.

If the system is submitted to a driving force F, a quantity of energy $\pm F\xi/2$ is imparted to the particle in the form of work during an elementary contact line movement. The plus (minus) sign arises when the motion is in (opposite to) the direction of the force. As a consequence, the contact line moves with an average velocity $U = \xi(\nu_+ - \nu_-)$, determined by the net frequency of forward and reverse jumps $\nu_\pm = \nu_0 \exp(\frac{-E^* \pm F\xi/2}{k_B T})$. For a contact line with nonequilibrium angle θ, the unbalanced capillary force reads $F = \gamma\xi(\cos\theta_e - \cos\theta)$. This leads to the central result of MKT (Blake & Haynes 1969):

$$U = 2\nu_0 \xi \exp\left(-\frac{E^*}{k_B T}\right) \sinh\left[\frac{\gamma\xi^2(\cos\theta_e - \cos\theta)}{2k_B T}\right]. \quad (15)$$

This relation predicts the contact line speed as a function of the driving force $\cos\theta_e - \cos\theta$. We emphasize that θ must be interpreted as a truly microscopic contact angle, defined on a molecular scale ξ, which is fundamentally different from the apparent (macroscopic) contact angle θ_{ap}. In the hierarchy of scales in **Figure 3*c***, the angle θ applies to the close-up on molecular scales, whereas θ_{ap} applies to the largest-scale meniscus profile.

The arguments of the Boltzmann factors in Equation 15 scale with $\gamma\xi^2/k_B T = (\xi/\ell_T)^2$. In the original interpretation of MKT, this ratio of length scales is of order unity. Hence one can approximate $\sinh(x) \simeq x$ and recover a linear relation between the speed and driving force (Seveno et al. 2009). In this interpretation, MKT does not represent any contact angle hysteresis: The limit of vanishing velocity gives the same value for θ_e both for advancing contact lines ($U \downarrow 0$) and for receding contact lines ($U \uparrow 0$).

5.2.2. Relation to Eyring's viscosity. MKT is based on the same principles as Eyring's phenomenological theory for the viscosity of liquids (Blake & De Coninck 2011). In a bulk liquid, ξ is interpreted as the size of a molecular rearrangement, induced by a shear stress τ. Taking $F = \tau\xi^2$,

and following the steps of the preceding paragraph, one obtains Eyring's formula for the liquid viscosity:

$$\eta = \frac{k_B T}{v_0 \xi^3} \exp\left(\frac{E_\eta}{k_B T}\right). \tag{16}$$

The activation energy E_η results from liquid-liquid interactions and can be estimated by the liquid-liquid adhesion energy $E_\eta \sim 2\gamma\xi^2$. This phenomenological description provides a realistic estimate for the viscosity of simple liquids (Monnery et al. 1995). Note that the polymeric liquids standardly used in labs to reach high viscosities (e.g., glycerol) cannot be described by Eyring's viscosity model as they present a glassy dynamics.

Combining the Eyring viscosity with the linearized MKT, Equation 15 gives

$$U = \frac{\gamma}{\eta} \exp\left(\frac{E_\eta - E^*}{k_B T}\right)(\cos\theta_e - \cos\theta). \tag{17}$$

The energy $E_\eta - E^*$ appearing in the Boltzmann factor is typically of the order of $\gamma\xi^2(1 - \cos\theta_e)$ such that the Boltzmann factors are once more of order unity. As the viscosity appears explicitly in Equation 17, MKT can be interpreted in a hydrodynamic framework. On the scale of the first molecular layers, the balance of viscous stress and capillary force would induce a bending of the surface by an amount $\cos\theta_e - \cos\theta \sim \mathrm{Ca}$. This relation is of the same form as Equation 14, except that the ratio ζ/ℓ_s is replaced by a Boltzmann factor of order unity. From this perspective, MKT should not be considered as an alternative to the hydrodynamical description, but as a particular slip model for the molecular-scale boundary condition.

5.2.3. Dissipation induced by surface heterogeneities. Substrates generically present heterogeneities of chemical or geometrical origin. These heterogeneities can be modeled as effective energy barriers, which have a characteristic width ξ and height E^*. Although not designed for that purpose, the MKT model turns out to provide an effective description of contact line motion due to activated processes in the presence of substrate heterogeneities (Prevost et al. 1999, Rolley & Guthmann 2007). **Figure 7*a*** shows the velocity of a moving contact line as a function of the apparent contact angle in the vicinity of the threshold of depinning. Over a very small range of apparent contact angles (approximately 2°), one observes an exponential increase of the velocity. This is consistent with the thermal activation model of Equation 15, provided that $\xi/\ell_T \gg 1$. A fit of the experimental data reveals an activation length scale ξ of typically 10 nm, which is at least one order of magnitude larger than ℓ_T. Introducing the dimensionless number $H = E^*/\gamma\xi^2$, one can write the MKT as

$$U \simeq 2v_0\xi \exp\left(-\frac{\xi^2}{\ell_T^2}[H + \cos\theta_e - \cos\theta]\right). \tag{18}$$

Bearing in mind that $(\xi/\ell_T)^2 \simeq 10^3$, this expression predicts a quasi-discontinuity of the microscopic contact angle across $\mathrm{Ca} = 0$: The contact line velocity can become significant only when the energy barriers disappear, for $\cos\theta \simeq \cos\theta_e \pm H$. Therefore, H is naturally interpreted as the contact angle hysteresis: $H = \frac{1}{2}(\cos\theta_r - \cos\theta_a)$, where $\theta_{a,r}$ are the advancing and receding contact angles. Because the length scale of the activation is now much larger than ℓ_T, one can no longer interpret v_0 as the thermal attempt frequency. Following Kramers's analysis (Hanggi et al. 1990, Kramers 1940), the attempt frequency v_0 is given by the well oscillation frequency $v_0 \sim \sqrt{\gamma H/\rho\xi^3}$ in the underdamped regime and by the dissipative frequency $v_0 \sim H\gamma/\eta\xi$ in the overdamped regime. Both estimates are approximately 10^9 Hz for typical experiments.

6. DYNAMICAL WETTING REGIMES

In this concluding section we propose an organization of the different regimes of contact line motion.

6.1. Hydrodynamic Versus Thermally Activated Regime

The motion of contact lines can be deduced from a balance between the power generated by capillary forces and the total energy dissipation taking place at different scales. There is substantial direct evidence that, beyond the threshold of contact angle hysteresis, the motion is dominated by viscous dissipation. (*a*) The predicted logarithmic variation of the interface slope with distance to the contact line is observed over one decade (**Figure 4*a***). (*b*) The phenomenology of dynamical wetting transitions can, and can only, be recovered using hydrodynamics (**Figure 4*b***). (*c*) The radius of curvature at the back of a V-shaped drop is observed to vary exponentially with the capillary number over one decade (**Figure 5**). (*d*) At low Reynolds numbers, the hydrodynamics describes quantitatively all experimental results, within an uncertainty that is comparable to the hysteresis (**Figures 4–6**). This implies that the dominant dissipation is spread over six decades of length scales (from 1 nm to macroscopic distances to the contact line) and that molecular processes essentially appear as cutoffs to the dissipation. The tests cited above are much more delicate than the classical measurement of θ_{ap} versus speed: The dynamic contact angle can usually be fitted accurately by more than one model (Le Grand et al. 2005, Seveno et al. 2009).

At low capillary numbers, close to the threshold of depinning, molecular-scale processes generically become dominant owing to surface heterogeneities. Indeed, even for the best physicochemical coating that can be realized, the hysteresis is still approximately 1% so that the Boltzmann factor appearing in Equation 18 is always much larger than unity. In this limit, the contact line motion occurs by thermal activation (**Figure 7*a***). It is accurately described by MKT, provided that the

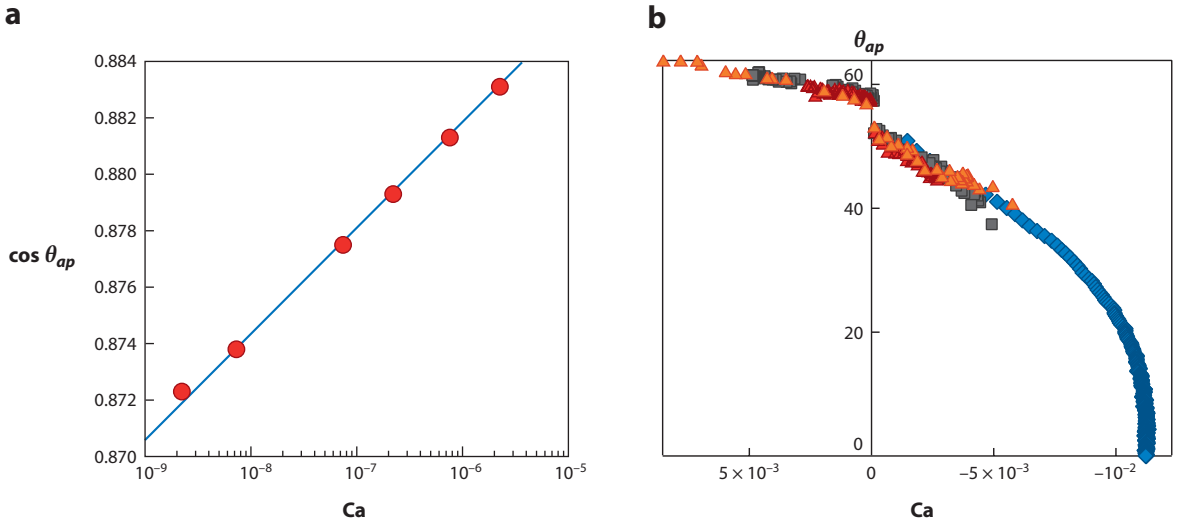

Figure 7

(*a*) Relation between the apparent contact angle θ_{ap} and the capillary number Ca in a dip-coating experiment performed with liquid hydrogen on a cesium substrate. The exponential dependence on velocity is the signature of a thermally activated regime below Ca $= 10^{-5}$. Data taken from Rolley & Guthmann (2007). (*b*) Same as in panel *a* but for silicon oil on a fluorinated substrate (*blue symbols*; Delon et al. 2008) and for a drop of the same fluid flowing down an inclined plane (*red*, *orange*, *and gray symbols*; Rio et al. 2005). The quantitative agreement with the multiscale lubrication theory (**Figure 4*b***) points to a hydrodynamic regime above Ca $= 10^{-4}$.

ratio of jump size and thermal length ξ/ℓ_T is much larger than unity. There are two noticeable exceptions for which ξ/ℓ_T could be of order unity such that there is no hysteresis: liquid lenses, for which the substrate is not solid but consists of a liquid layer, or nearly perfectly homogeneous substrates in molecular dynamics simulations.

The crossover between the thermally activated regime and the hydrodynamic regime takes place around the depinning transition ($\cos\theta \simeq \cos\theta_e \pm H$) at which the energy barriers vanish. **Figure 7*b*** shows experimental measurements of apparent contact angles in the hydrodynamic regime. One can clearly see the hysteretic gap in θ_{ap} at very small Ca, which is the range in which contact line motion is thermally activated. For future work, it will be interesting to observe thermally activated–contact line motion and the hydrodynamic regime in a single experimental setup—comparing the data in **Figure 7*a*,*b***, the crossover is expected between Ca $\sim 10^{-5}$ and 10^{-4}.

6.2. Inertial Effects

Another transition takes place when inertial effects become comparable to viscous effects. **Figure 8** shows an extreme situation—the initial phase of the spreading of a water drop—which is totally

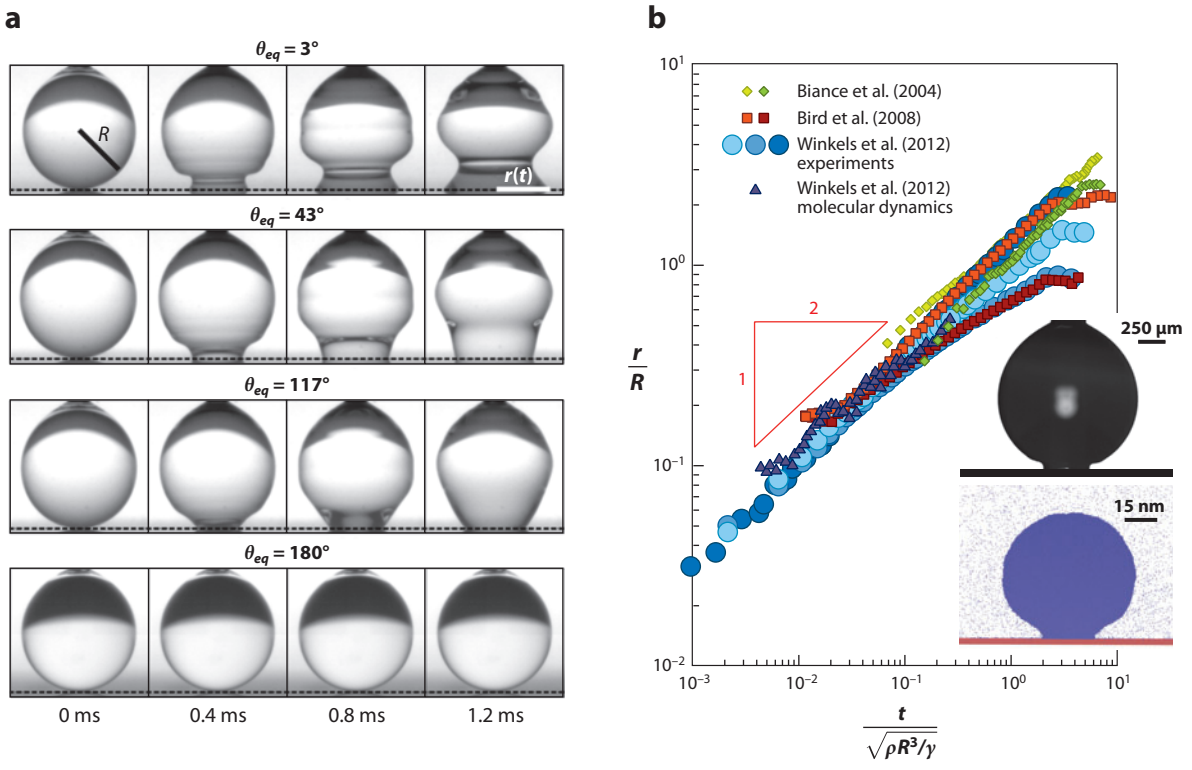

Figure 8

(*a*) Inertial spreading of water drops of radius $R = 0.82$ mm on different surfaces. Panel *a* adapted with permission from Bird et al. (2008). Copyright 2008 by the American Physical Society. (*b*) Contact radius r as a function of time t for different equilibrium contact angles. Different colors correspond to different drop sizes. Data taken from Biance et al. (2004) (*diamonds*), Bird et al. (2008) (*squares*), and Winkels et al. (2012) (*circles* and *triangles* correspond to experiments and molecular dynamics, respectively). The time is rescaled by the inertial time $\sqrt{\rho R^3/\gamma}$ based on density ρ and surface tension. The red triangle shows the scaling exponent 1/2. (*Insets*) Initial stages of drop spreading for a water drop (*top*) and for a simulated Lennard-Jones drop (*bottom*). Figure adapted with permission from Winkels et al. (2012). Copyright 2012 by the American Physical Society.

controlled by inertia (Biance et al. 2004, Bird et al. 2008, Winkels et al. 2012). Moreover, the splashing in **Figure 1** clearly involves inertial effects. To address the crossover between viscous and inertial regimes, one can add perturbatively the inertial effect to the lubrication equation, which can be interpreted as a depth-averaged (Saint-Venant) equation. This method was previously used in the context of Landau-Levich films (Koulago et al. 1995) and shows that inertia provides additional dissipation when a plate is withdrawn. Cox (1998) followed another approach using a perturbation expansion, which was qualitatively (not quantitatively) confirmed experimentally (Stoev et al. 1999). It remains to be investigated whether the effect of inertia could explain the differences when comparing low-viscosity fluids such as water to silicon oils (Podgorski et al. 2001, Winkels et al. 2011).

FUTURE ISSUES

1. The systematic procedure to capture the hydrodynamic and thermally activated regimes in a single description is to solve fluctuating hydrodynamics (Flekkoy & Rothman 1996). Is this feasible in the context of moving contact lines?
2. The activated–contact line motion involves an activation length ξ of approximately 10 nm. What determines the activation surface ξ^2? How is it correlated with the surface roughness, density of defects, and/or with collective effects (Le Doussal et al. 2009)?
3. New challenges for moving contact lines emerge from the influence of additional mechanisms, such as the inclusion of liquid inertia.
4. Strong evaporation can affect the contact line motion. In particular, if the liquid contains a solute such as polymers or colloids, this leads to stick slip and patterning (**Figure 2**).
5. Another type of complexity is related to the substrates. Contact line motion can be greatly influenced, e.g., by patterns on superhydrophobic surfaces (Roach et al. 2008).
6. If the substrate is a soft solid that can be deformed by capillarity, dissipation can be dominated by the viscoelastic behavior of the solid (Carre et al. 1996). How is the contact line motion influenced if the substrate is swelling, such as a gel or elastomer?

DISCLOSURE STATEMENT

The authors are not aware of any biases that might be perceived as affecting the objectivity of this review.

ACKNOWLEDGMENTS

We thank L. Bocquet, K. Davitt, J. Eggers, L. Limat, and E. Rolley for extensive discussions.

LITERATURE CITED

Abkarian M, Nunes J, Stone HA. 2004. Colloidal crystallization and banding in a cylindrical geometry. *J. Am. Chem. Soc.* 126:5978–79

Andrew MK, Harris PD. 1995. Damping and gas viscosity measurements using a microstructure. *Sens. Actuators A* 49:103–8

Ben Amar M, Cummings LJ, Pomeau Y. 2003. Transition of a moving contact line from smooth to angular. *Phys. Fluids* 15:2949–60

Benkreira H, Ikin JB. 2010. Dynamic wetting and gas viscosity effects. *Chem. Eng. Sci.* 65:1790–96

Benkreira H, Khan MI. 2008. Air entrainment in dip coating under reduced air pressures. *Chem. Eng. Sci.* 63:448–59
Berteloot G, Pham CT, Daerr A, Lequeux F, Limat L. 2008. Evaporation-induced flow near a contact line: consequences on coating and contact angle. *Europhys. Lett.* 83:14003
Biance AL, Clanet C, Quéré D. 2004. First steps of the spreading of a liquid droplet. *Phys. Rev. E* 69:016301
Bird JC, Mandre S, Stone HA. 2008. Short-time dynamics of partial wetting. *Phys. Rev. Lett.* 100:234501
Blake TD. 2006. The physics of moving wetting lines. *J. Colloid Interface Sci.* 299:1–13
Blake TD, De Coninck J. 2011. Dynamics of wetting and Kramers' theory. *Eur. Phys. J. Spec. Top.* 197:249–64
Blake TD, Haynes JM. 1969. Kinetics of liquid/liquid displacement. *J. Colloid Interface Sci.* 30:421–23
Blake TD, Ruschak KJ. 1979. A maximum speed of wetting. *Nature* 282:489–91
Bocquet L. 1993. Slipping of a fluid on a surface of controlled roughness. *C. R. Acad. Sci. II* 316:7–12
Bocquet L, Charlaix E. 2010. Nanofluidics, from bulk to interfaces. *Chem. Soc. Rev.* 39:1073–95
Bonn D, Eggers J, Indekeu J, Meunier J, Rolley E. 2009. Wetting and spreading. *Rev. Mod. Phys.* 81:739–805
Brochard-Wyart F, di Meglio JM, Quéré D. 1987. Dewetting: growth of dry regions from a film covering a flat solid or a fiber. *C. R. Acad. Sci. II* 304:553–58
Buckingham R, Shearer M, Bertozzi A. 2003. Thin film traveling waves and the Navier slip condition. *SIAM J. Appl. Math.* 63:722–44
Burley R, Kennedy BS. 1976. Study of dynamic wetting behavior of polyester tapes. *Br. Polym. J.* 8:140–43
Carlson A, Do-Quang M, Amberg G. 2009. Modeling of dynamic wetting far from equilibrium. *Phys. Fluids* 21:121701
Carre A, Gastel J, Shanahan M. 1996. Viscoelastic effects in the spreading of liquids. *Nature* 379:432–34
Cazabat AM, Guena G. 2010. Evaporation of macroscopic sessile droplets. *Soft Matter* 6:2591–612
Chan TS, Gueudre T, Snoeijer JH. 2011. Maximum speed of dewetting on a fiber. *Phys. Fluids* 23:112103
Chan TS, Snoeijer JH, Eggers J. 2012. Theory of the forced wetting transition. *Phys. Fluids* 24:07 2104
Colinet P, Rednikov A. 2011. On integrable singularities and apparent contact angles within a classical paradigm: partial and complete wetting regimes with or without phase change. *Eur. Phys. J. Spec. Top.* 197:89–113
Cox RG. 1986. The dynamics of the spreading of liquids on a solid surface. Part 1. Viscous flow. *J. Fluid Mech.* 168:169–94
Cox RG. 1998. Inertial and viscous effects on dynamic contact angles. *J. Fluid Mech.* 357:249–78
Craster RV, Matar OK. 2009. Dynamics and stability of thin liquid films. *Rev. Mod. Phys.* 81:1131–98
de Feijter JA. 1988. Thermodynamics of thin liquid films. In *Thin Liquid Films*, ed. IB Ivanov, pp. 1–47. New York: Marcel Dekker
de Gennes PG. 1985. Wetting: statics and dynamics. *Rev. Mod. Phys.* 57:827–63
de Gennes PG. 1986. Transformation process for a horizontal soap film. *C. R. Acad. Sci. II* 303:1275–77
de Gennes PG, Brochart-Wyart F, Quéré D, eds. 2002. *Gouttes, Bulles, Perles et Ondes.* Paris: Belin
de Gennes PG, Hua X, Levinson P. 1990. Dynamics of wetting: local contact angles. *J. Fluid Mech.* 212:55–63
De Ruiter J, Oh JM, van den Ende D, Mugele F. 2012. Dynamics of collapse of air films in drop impact. *Phys. Rev. Lett.* 108:074505
Deegan RD, Bakajin O, Dupont TF, Huber G, Nagel SR, Witten TA. 1997. Capillary flow as the cause of ring stains from dried liquid drops. *Nature* 389:827–29
Delon G, Fermigier M, Snoeijer JH, Andreotti B. 2008. Relaxation of a dewetting contact line. Part 2: Experiments. *J. Fluid Mech.* 604:55–75
Deryaguin BV. 1943. On the thickness of a layer of liquid remaining on the walls of vessels after their emptying, and the theory of the application of photoemulsion after coating on the cine film. *Acta Physicochim. USSR* 20:349
Deryaguin BV, Levi SM. 1964. *Film Coating Theory*. London: Focal
Do-Quang M, Amberg G. 2009. The splash of a solid sphere impacting on a liquid surface: numerical simulation of the influence of wetting. *Phys. Fluids* 21:022102
Duez C, Ybert C, Clanet C, Bocquet L. 2007. Making a splash with water repellency. *Nat. Phys.* 3:180–83
Duffy BR, Wilson SK. 1997. A third-order differential equation arising in thin-film flows and relevant to Tanner's law. *Appl. Math. Lett.* 10:63–68

Dussan V EB. 1979. Spreading of liquids on solid surfaces: static and dynamic contact lines. *Annu. Rev. Fluid Mech.* 11:371–400

Dussan V EB, Davis SH. 1974. On the motion of a fluid-fluid interface along a solid surface. *J. Fluid Mech.* 65:71–95

Eggers J. 2004. Hydrodynamic theory of forced dewetting. *Phys. Rev. Lett.* 93:094502

Eggers J. 2005a. Contact line motion for partially wetting fluids. *Phys. Rev. E* 72:061605

Eggers J. 2005b. Existence of receding and advancing contact lines. *Phys. Fluids* 17:082106

Eggers J, Stone HA. 2004. Characteristic lengths at moving contact lines for a perfectly wetting fluid: the influence of speed on the dynamic contact angle. *J. Fluid Mech.* 505:309–21

Flekkoy E, Rothman D. 1996. Fluctuating hydrodynamic interfaces: theory and simulation. *Phys. Rev. E* 53:1622–43

Flitton JC, King JR. 2004. Surface-tension-driven dewetting of Newtonian and power-law fluids. *J. Eng. Math.* 50:241–66

Getta T, Dietrich S. 1998. Line tension between fluid phases and a substrate. *Phys. Rev. E* 57:655–71

Golestanian R, Raphaël E. 2001. Dissipation in the dynamics of a moving contact line. *Phys. Rev. E* 64:031601

Hanggi P, Talkner P, Borkovec M. 1990. Reaction-rate theory: 50 years after Kramers. *Rev. Mod. Phys.* 62:251–341

Hocking LM. 1983. The spreading of a thin drop by gravity and capillarity. *Q. J. Mech. Appl. Math.* 36:55–69

Huang DM, Sendner C, Horinek D, Netz RR, Bocquet L. 2008. Water slippage versus contact angle: a quasiuniversal relationship. *Phys. Rev. Lett.* 101:226101

Huh C, Scriven LE. 1971. Hydrodynamic model of steady movement of a solid/liquid/fluid contact line. *J. Colloid Interface Sci.* 35:85–101

Jacqmin D. 2000. Contact-line dynamics of a diffuse fluid interface. *J. Fluid Mech.* 402:57–88

Kavehpour HP, Ovryn B, McKinley GH. 2003. Microscopic and macroscopic structure of the precursor layer in spreading viscous drops. *Phys. Rev. Lett.* 91:196104

Kirkwood J, Buff F. 1949. The statistical mechanical theory of surface tension. *J. Chem. Phys.* 17:338–43

Koulago A, Shkadov V, Quéré D, Deryck A. 1995. Film entrained by a fiber quickly drawn out of a liquid bath. *Phys. Fluids* 7:1221–24

Kramers H. 1940. Brownian motion in a field of force and the diffusion model of chemical reactions. *Physica* 7:284–304

Landau LD, Levich BV. 1942. Dragging of a liquid by a moving plate. *Acta Physicochim. USSR* 17:42

Landau LD, Lifshitz EM. 1984. *Fluid Mechanics*. Oxford: Pergamon

Le Doussal P, Wiese KJ, Moulinet S, Rolley E. 2009. Height fluctuations of a contact line: a direct measurement of the renormalized disorder correlator. *Europhys. Lett.* 87:56001

Le Grand N, Daerr A, Limat L. 2005. Shape and motion of drops sliding down an inclined plane. *J. Fluid Mech.* 541:293–315

Ledesma-Aguilar R, Nistal R, Hernández-Machado A, Pagonabarraga I. 2011. Controlled drop emission by wetting properties in driven liquid filaments. *Nat. Mater.* 10:367–71

Limat L, Stone HA. 2004. Three-dimensional lubrication model of a contact line corner singularity. *Europhys. Lett.* 65:365–71

Maleki M, Reyssat E, Quéré D, Golestanian R. 2007. On the Landau-Levich transition. *Langmuir* 23:10116–22

Mandre S, Mani M, Brenner MP. 2009. Precursors to splashing of liquid droplets on a solid surface. *Phys. Rev. Lett.* 102:134502

Marchand A, Chan TS, Snoeijer JH, Andreotti B. 2012. Air entrainment by contact lines of a solid plate plunged into a viscous liquid. *Phys. Rev. Lett.* 108:204501

Maxwell J. 1878. On stresses in rarified gases arising from inequalities of temperature. *Philos. Trans. R. Soc. Lond.* 170:231–56

Merchant G, Keller J. 1992. Contact angles. *Phys. Fluids A* 4:477–85

Moffat JR, Sefiane K, Shanahan MER. 2009. Effect of TiO_2 nanoparticles on contact line stick-slip behavior of volatile drops. *J. Phys. Chem. B* 113:8860–66

Monnery W, Svrcek W, Mehrotra A. 1995. Viscosity: a critical review of practical predictive and correlative methods. *Can. J. Chem. Eng.* 73:3–40

Morris D, Hannon L, Garcia A. 1992. Slip length in a dilute gas. *Phys. Rev. A* 46:5279–81
Mugele F, Baret JC. 2005. Electrowetting: from basics to applications. *J. Phys. Condens. Matter* 17:R705–74
Nikolayev V, Beysens D. 2003. Equation of motion of the triple contact line along an inhomogeneous surface. *Europhys. Lett.* 64:763–68
Oron A, Davis SH, Bankoff SG. 1997. Long-scale evolution of thin liquid films. *Rev. Mod. Phys.* 69:931–80
Peters I, Snoeijer JH, Daerr A, Limat L. 2009. Coexistence of two singularities in dewetting flows: regularizing the corner tip. *Phys. Rev. Lett.* 103:114501
Pismen LM. 2001. Nonlocal diffuse interface theory of thin films and moving contact line. *Phys. Rev. E* 64:021603
Pismen LM, Eggers J. 2008. Solvability condition for the moving contact line. *Phys. Rev. E* 78:056302
Pismen LM, Pomeau Y. 2000. Disjoining potential and spreading of thin layers in the diffuse interface model coupled to hydrodynamics. *Phys. Rev. E* 62:2480–92
Podgorski T, Flesselles JM, Limat L. 2001. Corners, cusps, and pearls in running drops. *Phys. Rev. Lett.* 87:036102
Prevost A, Rolley E, Guthmann C. 1999. Thermally activated motion of the contact line of a liquid helium-4 meniscus on a cesium substrate. *Phys. Rev. Lett.* 83:348–51
Qian T, Wang XP, Sheng P. 2004. Power-law slip profile of the moving contact line in two-phase immiscible flows. *Phys. Rev. Lett.* 93:094501
Qian T, Wang XP, Sheng P. 2006. A variational approach to moving contact line hydrodynamics. *J. Fluid Mech.* 564:333–60
Quéré D. 1991. On the minimal velocity of forced spreading in partial wetting. *C. R. Acad. Sci. II* 313:313–18 (In French)
Ramé E, Garoff S. 1996. Microscopic and macroscopic dynamic interface shapes and the interpretation of dynamic contact angles. *J. Colloid Interface Sci.* 177:234–44
Redon C, Brochard-Wyart F, Rondelez F. 1991. Dynamics of dewetting. *Phys. Rev. Lett.* 66:715–18
Reiter G. 1992. Dewetting of thin polymer films. *Phys. Rev. Lett.* 68:75–78
Ren W, E W. 2007. Boundary conditions for the moving contact line problem. *Phys. Fluids* 19:022101
Rio E, Daerr A, Andreotti B, Limat L. 2005. Boundary conditions in the vicinity of a dynamic contact line: experimental investigation of viscous drops sliding down an inclined plane. *Phys. Rev. Lett.* 94:024503
Roach P, Shirtcliffe NJ, Newton MI. 2008. Progress in superhydrophobic surface development. *Soft Matter* 4:224–40
Rolley E, Guthmann C. 2007. Dynamics and hysteresis of the contact line between liquid hydrogen and cesium substrates. *Phys. Rev. Lett.* 98:166105
Rowlinson JS, Widom B. 1982. *Molecular Theory of Capillarity*. Oxford: Clarendon
Saulnier F, Raphaël E, de Gennes PG. 2002. Dewetting of thin polymer films near the glass transition. *Phys. Rev. Lett.* 88:196101
Schwartz LW, Roux D, Cooper-White JJ. 2005. On the shapes of droplets that are sliding on a vertical wall. *Physica D* 209:236–44
Sedev RV, Petrov JG. 1991. The critical condition for transition from steady wetting to film entrainment. *Colloids Surf.* 53:147–56
Seemann R, Herminghaus S, Jacobs K. 2001. Dewetting patterns and molecular forces: a reconciliation. *Phys. Rev. Lett.* 86:5534–37
Seveno D, Dinter N, De Coninck J. 2010. Wetting dynamics of drop spreading: new evidence for the microscopic validity of the molecular-kinetic theory. *Langmuir* 26:14642–47
Seveno D, Vaillant A, Rioboo R, Adao H, Conti J, De Coninck J. 2009. Dynamics of wetting revisited. *Langmuir* 25:13034–44
Simpkins PG, Kuck VJ. 2000. Air entrapment in coatings by way of a tip-streaming meniscus. *Nature* 403:641–43
Snoeijer J, Le Grand N, Limat L, Stone HA, Eggers J. 2007a. Cornered drop and rivulets. *Phys. Fluids* 19:042104
Snoeijer JH. 2006. Free surface flows with large slopes: beyond lubrication theory. *Phys. Fluids* 18:021701
Snoeijer JH, Andreotti B. 2008. A microscopic view on contact angle selection. *Phys. Fluids* 20:057101

Snoeijer JH, Andreotti B, Delon G, Fermigier M. 2007b. Relaxation of a dewetting contact line. Part 1: A full-scale hydrodynamic calculation. *J. Fluid Mech.* 579:63–83

Snoeijer JH, Delon G, Fermigier M, Andreotti B. 2006. Avoided critical behavior in dynamically forced wetting. *Phys. Rev. Lett.* 96:174504

Snoeijer JH, Eggers J. 2010. Asymptotics of the dewetting rim. *Phys. Rev. E* 82:056314

Stoev K, Ramé E, Garoff S. 1999. Effects of inertia on the hydrodynamics near moving contact lines. *Phys. Fluids* 11:3209–16

Thiele U. 2003. Open questions and promising new fields in dewetting. *Eur. Phys. J. E* 12:409–16

Thiele U, Neuffer K, Bestehorn M, Pomeau Y, Velarde MG. 2002. Sliding drops on an inclined plane. *Colloid Surf. A* 206:87–104

Tsai P, van der Veen RCA, van de Raa M, Lohse D. 2010. How micropatterns and air pressure affect splashing on surfaces. *Langmuir* 26:16090–95

Voinov OV. 1976. Hydrodynamics of wetting. *Fluid Dyn.* 11:714–21

Watanabe S, Inukai K, Mizuta S, Miyahara MT. 2009. Mechanism for stripe pattern formation on hydrophilic surfaces by using convective self-assembly. *Langmuir* 25:7287–95

Winkels K, Weijs JH, Eddi A, Snoeijer JH. 2012. Initial spreading of low-viscosity drops on partially wetting surfaces. *Phys. Rev. E* 85:055301

Winkels KG, Peters IR, Evangelista F, Riepen M, Daerr A, et al. 2011. Receding contact lines: from sliding drops to immersion lithography. *Eur. Phys. J. Spec. Top.* 192:195–205

Xu L, Zhang WW, Nagel SR. 2005. Drop splashing on a dry smooth surface. *Phys. Rev. Lett.* 94:184505

Young T. 1805. An essay on the cohesion of fluids. *Philos. Trans. R. Soc. Lond.* 95:65–87

Yue P, Feng JJ. 2011. Can diffuse-interface models quantitatively describe moving contact lines? *Eur. Phys. J. Spec. Top.* 197:37–46

Annual Review of
Fluid Mechanics

Volume 45, 2013

Contents

Indexes

Errata

An online log of corrections to *Annual Review of Fluid Mechanics* articles may be found at http://fluid.annualreviews.org/errata.shtml